

# Resolving the Structure at the Heart of BAL Quasars Through Microlensing Induced Polarisation Variability

Christopher A. Hales<sup>A,B</sup> and Geraint F. Lewis<sup>A</sup>

<sup>A</sup> Institute of Astronomy, School of Physics, University of Sydney, Sydney NSW 2006, Australia

<sup>B</sup> Corresponding author. Email: chales@physics.usyd.edu.au

Received 2006 December 13, accepted 2007 March 13

**Abstract:** While amongst the most luminous objects in the universe, many details regarding the inner structure of quasars remain unknown. One such area is the mechanism promoting increased polarisation in the broad absorption line troughs of certain quasars. This study shows how microlensing can be used to differentiate between two popular models that explain such polarisation through a realistic computational analysis. By examining a statistical ensemble of correlation data between two observables (namely image brightness and polarisation of the flux coming from the quasar), it was found that through spectropolarimetric monitoring it would be possible to discern between a model with an external scattering region and a model without one.

**Keywords:** galaxies: structure — gravitational lensing — polarisation — quasars: individual (H1413+1143)

## 1 Introduction

Quasars are amongst the most luminous objects in the universe, radiating most of their energy from within a small continuum emitting region only  $\sim 1$  pc in extent. Such a source at cosmological distances subtends the order of microarcseconds, well below the highest angular resolution obtainable with modern telescopes. However, gravitational microlensing can be employed to reveal the structure at the heart of quasars, with magnification due to individual stars revealing information about the size of the continuum emitting accretion disk (Wambsganss, Schneider & Paczynski 1990; Witt & Mao 1994; Hawkins & Taylor 1997; Gould & Miralda-Escudé 1997) and broad emission line region (Wyithe & Loeb 2002; Abajas et al. 2002; Lewis & Ibata 2004).

While the microlensing advances have improved our understanding of quasar structure, the picture is far from complete, especially with regards to areas such as the mechanism promoting jet activity, which in turn dictates radio-loudness or -softness, e.g. Kuncic (1999); Cattaneo (2002); Fender et al. (2004), and its relation to prominent absorbing regions (e.g. Murray et al. 1995; Lewis & Belle 1998). In particular, the exact mechanism which promotes increased polarisation in the broad absorption line (BAL) troughs of quasar spectra is not well understood. This paper will extend recent studies (Lewis & Belle 1998; Belle & Lewis 2000) to computationally simulate how gravitational microlensing can be used to discern between the two main models for polarisation enhancement and hence probe the scales of structure in the absorbing/scattering regions. Section 2 discusses the details of BAL quasars, microlensing, and the quadruply imaged quasar H1413+1143, the system which is the ideal

observational candidate for this study. Section 3 details the approach to the simulations, including the construction of the source profiles and polarisation maps, with the results and conclusions of this study presented in Sections 4 and 5 respectively.

## 2 Background

### 2.1 BAL Quasars and Polarisation

Approximately 10–20% of optically selected quasars have been found to exhibit broad absorption troughs in resonant lines blueward of the corresponding emission lines (Hewett & Foltz 2003; Reichard et al. 2003), exhibiting bulk outflow velocities of around  $5000\text{--}30000\text{ km s}^{-1}$ . (Turnshek 1984). These BAL quasars were thought to consist of only radio-quiet or radio-intermediate sources, but the discovery of a radio-loud BAL quasar suggests the phenomenon occurs throughout the quasar population (Becker et al. 1997). Current theories suggest an orientation-based unification scheme to explain the occurrence of the BAL in quasars (e.g. Antonucci 1993), and of interest to this study is the scattering structure which increases polarisation within BAL troughs.

Figure 1 shows the two competing models for explaining the enhanced polarisation in the broad absorption lines (Cohen et al. 1995; Ogle 1997; Schmidt & Hines 1999). For Model A, radiation from the nuclear region only travels along Path A through the BAL clouds. This radiation is then enhanced by resonant scattering into the line of sight, increasing the polarisation within the absorption troughs. For Model B, radiation travels along Paths A and B. However, in this case Path A does not necessarily introduce any increase in polarisation. Radiation travelling along

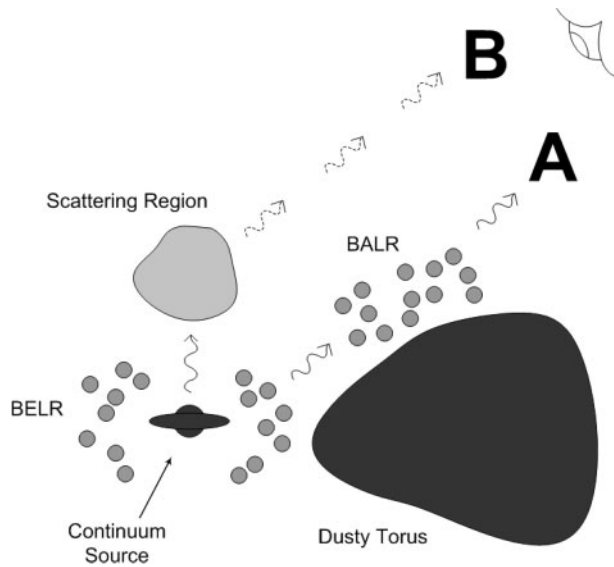


**Figure 1** The two potential models for the scattering and absorption structure (see explanation in Section 2.1, also Belle & Lewis 2000).

Path B is scattered into the line of sight, most likely from a region of electrons and dust (Antonucci & Miller 1985; Goodrich & Miller 1995; Gallagher et al. 1999; Brandt et al. 1999). Here, the increased polarisation in the absorption troughs is due to the reduced amount of unpolarised flux coming directly from the continuum along Path A (the polarised flux remains relatively free of absorption as it avoids the BAL clouds).

## 2.2 Microlensing

The details of gravitational lensing can be found in recent review articles (e.g. Wambsganss 1998) and only the salient features will be discussed here. Gravitational lensing occurs when light rays from a distant source pass near a massive object and suffer achromatic deflection. The deflection angle  $\alpha$  of such a light ray passing at a distance  $r$  from an object of mass  $m$  is given by Equation 1, i.e. light rays will follow null geodesics in the presence of massive objects.

$$\alpha = \frac{4Gm}{c^2 r} \quad (1)$$

The measurement of this deflection was one of the first key observational tests of Einstein's general relativity.

When considering the deflections due to individual galaxies, it is seen that multiple light paths can connect a source with an observer, resulting in multiple imaging on the scale of arcseconds. However, when small-scale granularity in the distribution of galactic matter (stars, planets, black holes) is considered, it is seen that these macrolensed images are actually composed of a myriad of unresolvable ( $\sim 10^{-6}$  arcsec) microimages due to imaging by stellar-mass objects (Chang & Refsdal 1979). While these microimages are unresolvable, the stellar-mass objects can introduce magnification of a background source, and the motions of the lensing stars can produce significant fluctuations into the observed brightness of the

macroimage. The characteristic scale length of microlensing is the Einstein Radius ( $ER$ ). For a point-mass lensing, and a perfect alignment of source ( $s$ ), lens ( $l$ ) and observer ( $o$ ), the result would be a circular image known as an Einstein Ring<sup>1</sup> at the Einstein Radius. The physical projection of this radius onto the source is given by Equation 2, where  $D$  is the angular diameter distance.

$$ER = \sqrt{\frac{4Gm}{c^2} \frac{D_{os} D_{ls}}{D_{ol}}} \quad (2)$$

The importance of this length scale is that objects smaller than it are much more susceptible to large magnifications, while objects larger than it suffer less magnification (Wambsganss & Paczynski 1991; Schneider, Ehlers & Falco 1999; Wambsganss 1992).

## 2.3 H1413+1143

H1413+1143 (the Cloverleaf) consists of four images of a  $z = 2.55$  quasar with angular separations of 0.77 to 1.36 arcsec (Magain et al. 1988; Turnshek et al. 1997). The lensing galaxy has only recently been identified (Kneib, Alloin & Pello 1998; Chantry & Magain 2007), with Magain et al. (1988) and Angonin et al. (1990) identifying two prominent absorption systems at  $z = 1.438$  and 1.661. For the purposes of this study, and for consistency with Lewis & Belle (1998), we adopt the mean of these two values,  $z = 1.55$ , to represent the redshift of the lensing galaxy. One of the images D (see Chartas et al. 2004), has been seen to exhibit variability consistent with microlensing (Angonin et al. 1990; Kayser et al. 1990; Østensen et al. 1997), with Hutsemékers (1993) suggesting that prominent differences in the absorption profiles of the images might be due to selective microlensing of absorbing clouds, with the scale size of these clouds being smaller than the continuum-forming region. It was conceded, however, that this would require a very precise lensing configuration. Furthermore, the polarisation for the summed images has been seen to vary in the blue wing of the C IV  $\lambda 1549$  emission line, with fluctuations between  $\sim 10\%$  (Lamy & Hutsemékers 2004) and  $\sim 20\%$  (Schmidt & Hines 1999). Interestingly, these studies also found that continuum polarisation near the C IV feature was  $\sim 2\%$ , indicating some polarisation is still occurring away from the absorption troughs (Wang, Wang & Wang 2005).

There seems to be growing support in the literature that an external, asymmetric scattering region is responsible for this polarisation increase (c.f. Model B in Section 2.1). A recent *HST* study of H1413+1143 (Chae et al. 2001) has indicated that the size scale for such a region lies approximately between the Einstein Ring size (i.e. Einstein diameter in the source plane) and  $10^{18} \sqrt{L_{46}}$  cm (where  $L_{46}$  is the lensed quasar luminosity in units of  $10^{46}$  ergs  $s^{-1}$ ). The minimum value comes from the requirement that the scattering region should not be as susceptible to microlensing as the central nucleus, whereas the maximum value is

<sup>1</sup> Despite being first proposed by Chwolson (1924).

simply an estimate for the size scale of the broad emission line region (BELR) (Murray & Chaing 1998; Kaspi et al. 2000). If the scattering region were any larger then the differences seen between macrolensed images would not be as great. Furthermore, recent data from *Chandra* (Chartas et al. 2004) appears to support this model.

By applying more realistic models for both the BAL region of H1413+1143 and the distribution of stars in the lensing galaxy, the observed spectral variations examined by Hutsemékers (1993) could be readily reproduced, removing the need for precise lensing configurations (Lewis & Belle 1998). This idea was furthered by Belle & Lewis (2000) who investigated the role that Models A and B (see Figure 1) might play in explaining the increased polarisation within BAL troughs. However, this previous study only tested one configuration with a scattering region scale size of half an Einstein radius. Hence, how secure are the conclusions drawn by Chae et al. (2001) and Chartas et al. (2004), and could Model A produce polarisation variations that could be misinterpreted as Model B? To this end, the remainder of this paper examines detailed simulations of both models and the predictions they make for polarisation variability.

### 3 Method

#### 3.1 Ray Tracing

When considering microlensing at cosmological scales, many stars influence the path of light through a galaxy, and the single, isolated lens approximation which works well in Galactic microlensing must be abandoned. Such a situation is analytically intractable and numerical techniques must be employed. This study employs the inverse/backwards ray-shooting technique (Kayser et al. 1990; Wambsganss 1990) which involves ‘shooting’ light rays from the observer to the lens plane, calculating the deflection due to individual stars in the lensing galaxy, and then collecting these rays in the pixels of the source plane where they eventually hit, forming a magnification map.

There are two main parameters required to model the microlensing which are dependent upon the mass distribution in the lensing galaxy: the dimensionless surface mass density  $\sigma$  (or optical depth) and the shear  $\gamma$  due to the large scale matter distribution. As these parameters are not strongly constrained for the Cloverleaf, this study has investigated four different models:  $\sigma = \gamma = 0.25$ , 0.4, 0.6 and 0.75. These were chosen because they represent a singular isothermal sphere, reasonably approximating the range of possible mass distributions for a lensing galaxy (Schneider, Ehlers & Falco 1999). Figure 2 shows example magnification maps for regions derived using the ray tracing method, with side lengths of  $10ER$  for the four cases of  $\sigma$  and  $\gamma$  above.

These maps can be scaled to physical distance using the Einstein radius (Equation 2). Assuming a standard cosmological model with  $h = 0.73$ ,  $\Lambda = 0.76$  and  $\Omega = 0.24$  (Spergel et al. 2007), and the lens and source redshifts given in Section 2.3,  $ER \approx 2.73 \times 10^{16}$  cm.

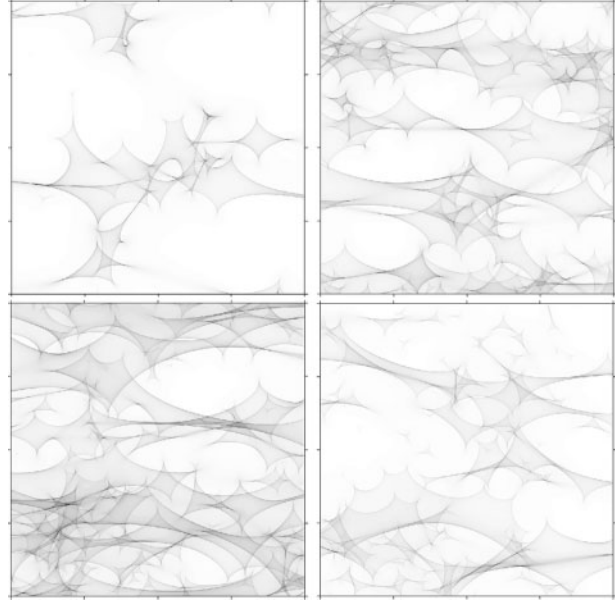


**Figure 2** Example magnification maps for  $\sigma = \gamma = 0.25$  (top left), 0.4 (top right), 0.6 (bottom left), and 0.75 (bottom right). Darker regions indicate higher magnification, with the sharp boundaries denoting caustics of the map. Each have dimension  $10 \times 10ER$ .

The magnifications due to microlensing fluctuate about a mean theoretical value given by

$$\mu_{\text{th}} = [(1 - \sigma^2) - \gamma^2]^{-1} \quad (3)$$

which is the magnification an image would suffer if the macrolens was composed of solely smooth matter. Hence, generally, the mean magnification over a large enough area should tend to this theoretically expected value. However, due to statistical variance, the mean value within an individual magnification map which is relatively small can deviate from this expected value (i.e. the smaller the region chosen, the larger the possible deviation from the mean theoretical magnification).

#### 3.2 Defining the Source

In order to determine the effect of microlensing on each model from Section 2.3, it was necessary to construct the image that the magnification map would ‘see’. This is shown schematically in Figure 3 and discussed in detail below.

##### 3.2.1 Absorption and Polarisation

In order to examine a BAL trough, Equation 4 was used to simulate the blue wing of CIV  $\lambda 1549$ , where  $\lambda_{\text{cc}} = 1505 \text{ \AA}$  is the wavelength at which 50% of the light from the continuum core is absorbed (corresponding to a bulk outflow at 50% absorption of  $\sim 8500 \text{ km s}^{-1}$ ) and  $2\Delta\lambda = 8.75 \text{ \AA}$  is the ‘width’ of the absorption feature between 27 and 73% absorption (Turnshek 1995; Weymann 1995).

$$A(\lambda) = \frac{1}{1 + \exp[(\lambda - \lambda_{\text{cc}})/\Delta\lambda]} \quad (4)$$

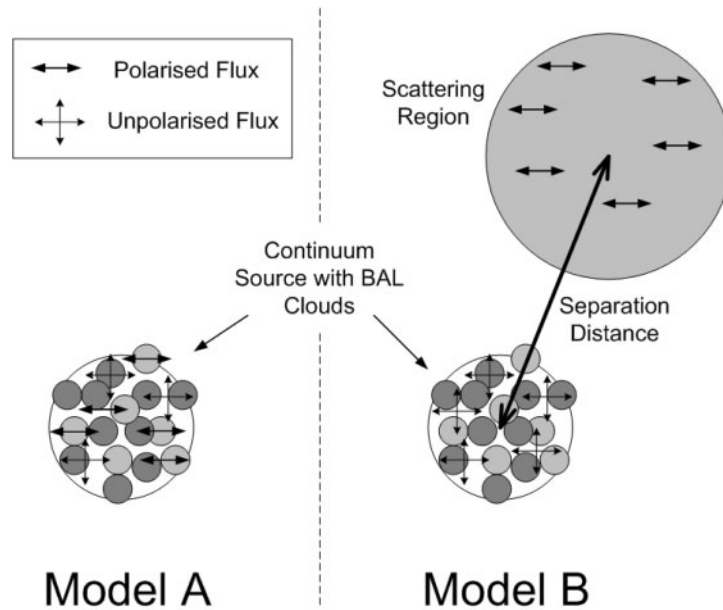


**Figure 3** Schematic view of the BAL quasar continuum and scattering region as seen by the microlensing magnification for both scattering scenarios. This is based on Figure 1 and is discussed further in Sections 3.2.2 and 3.2.3.

With regard to polarisation, as discussed in the following sections, the polarisation at any pixel was directly related to the absorption at that pixel. This could take on any value in the range from 0 to 20%. This would tend to generate conservative results for this study (note that, as mentioned in Section 2.3, the polarisation of the entire composite image could be as high as 20%); however, any general trends established here would still apply if a larger range for polarisation was used.

### 3.2.2 Model A: Scattering Within the BAL Region

For this study the quasar continuum source was modelled as a two-dimensional Gaussian surface with a brightness radius of  $10^{15}$  cm (Rees 1984; Blandford, Netzer & Woltjer 1990) on a  $64 \times 64$  pixel grid. The extent of this grid was defined so that the value of the Gaussian at the edges would be 10% or less than the value at the peak, giving a side length of  $3.65 \times 10^{15}$  cm (this kept the size of the grid down while allowing for good resolution). Hence, this Gaussian represents the unabsorbed continuum flux and in order to represent absorption, an absorption matrix (discussed shortly) would then be (dot) multiplied with the source grid (i.e. this absorption matrix is the same size as the source matrix).

In order to represent the scale length of the inhomogeneities in the BAL region (this will be referred to as cloud size), cloud sizes were set as  $3.65 \times 10^{15} \times 4^{-n}$  cm,  $n = 1, 2, 3$ . In this way, the smallest clouds were  $5.70 \times 10^{13}$  cm in extent ( $n = 3$ ) while the largest clouds were  $9.11 \times 10^{14}$  cm ( $n = 1$ ). This was implemented by limiting the initial matrix size for the absorption matrix generator and then drawing this matrix out to fill a  $64 \times 64$

grid. Note, this method was similar to that employed by Lewis & Belle (1998).

The absorption matrix represents the degree of variation of absorption about a particular wavelength (i.e. due to inhomogeneities in the density of the absorption region). The distribution of values were represented by a Gaussian of specified width  $\omega$  centred at  $A_c(\lambda)$ . A modification algorithm was developed to truncate this distribution outside the range 0–100%, and to reassign new values for the truncated elements such that the overall distribution of matrix values had mean  $\langle A(\lambda) \rangle$  and width  $\omega$ . The mean of the absorption distribution  $\langle A(\lambda) \rangle$  was chosen to be a function of wavelength as given by Equation 4. The algorithm was also designed so that if, for a particular  $\langle A(\lambda) \rangle$  and  $\omega$ ,  $A_c(\lambda)$  was located outside the 0–100% boundary, then  $A_c(\lambda)$  would be fixed at the boundary and  $\omega$  varied so as to ensure that  $\langle A(\lambda) \rangle$  was the value specified. This allows, for example, for a distribution with (mean) absorption of 10% and width of 50% to be generated so that all matrix values lie within 0–100%. For this paper, widths of 5% and 50% were investigated for absorption at 25%, 50% and 75%. Figure 4 shows how different cloud sizes were modelled with a particular set of absorption matrix parameters.

In order to implement polarisation, this image was then split into two separate images according to Equation 5. In this way, if Equation 6 was calculated at each pixel then the polarisation would be dependent on the particular absorption matrix value at that pixel. Here,  $Pix_n$  are the values at corresponding pixels in each new image,  $Pol_{unab} = 0.02$ ,  $Pol_{lim} = 0.18$ ,  $Abs$  is the absorption matrix value at that pixel, and  $Pol$  is the polarisation difference between the two images. In this way, if  $Abs = 0\%$  then  $Pol = 2\%$ ,

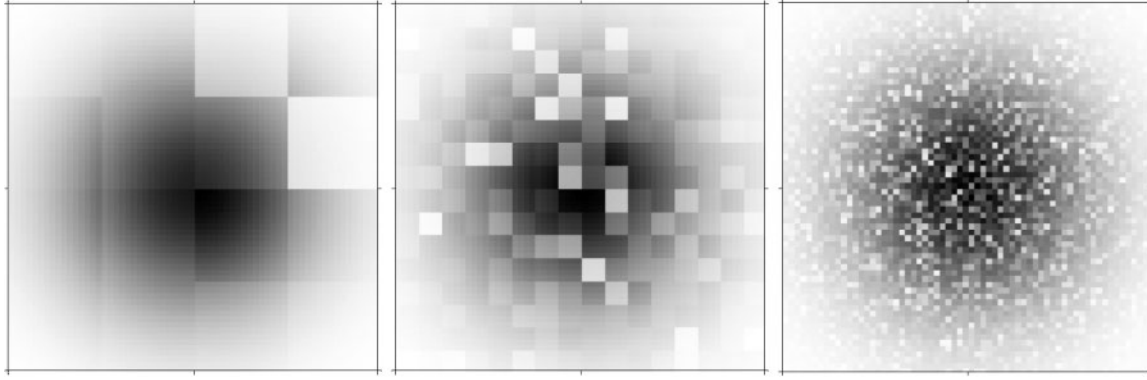


**Figure 4** Model A. Left: Source with cloudsize  $9.11 \times 10^{14}$  cm ( $n = 1$ ), absorption at 25% and  $\omega$  at 50%. Middle and Right: Same parameters but with cloudsize  $2.28 \times 10^{14}$  cm ( $n = 2$ ) and  $5.70 \times 10^{13}$  cm ( $n = 3$ ). Each have side length  $3.65 \times 10^{15}$  cm.

if  $Abs = 50\%$  then  $Pol = 11\%$ , and if  $Abs = 100\%$  then  $Pol = 20\%$ .

$$\begin{aligned} Pix_1 &= 0.5 P_{tot} (1 + Pol_{unab} + Pol_{lim} \times Abs) \\ Pix_2 &= 0.5 P_{tot} (1 - Pol_{unab} - Pol_{lim} \times Abs) \\ P_{tot} &= Pix_1 + Pix_2 \\ P_{dif} &= Pix_1 - Pix_2 \\ Pol &= \frac{P_{dif}}{P_{tot}} \end{aligned} \quad (5)$$

$$Pol = \frac{P_{dif}}{P_{tot}} \quad (6)$$

### 3.2.3 Model B: External Scattering Region

This model was somewhat constrained by the maximum magnification map that could be handled in terms of computer memory, so by setting this map with a side length of  $100ER$  ( $1024 \times 1024$  pixels) the pixel scale size was automatically set for any source models created. Fortunately this did not seriously affect the range of scattering region scale sizes that needed to be investigated. Unlike Model A, an absorption matrix was not required here (the continuum region is on the order of a few pixels), but rather absorption simply involved reducing the flux of the continuum while keeping the flux of the scattering region constant.

This left two main variables to manipulate besides absorption: the scale size of the scattering region and the separation distance of this region from the continuum. Note that the latter is in fact intrinsically linked to the scale size of the scattering region in that at scale sizes approaching the upper limit, the separation distance must be of the order of the scattering region radius (geometries where the separation distance is less than the scattering region radius would give similar correlation results). The scattering region radii and separation distances investigated for this model are shown in Figure 5. This involved setting the source as a  $64 \times 64$  grid for the smallest scattering region and  $200 \times 200$  for the larger two regions (resulting in much higher computation times). Also note that, like the continuum region in Model A, both the continuum and scattering regions in Model B were modelled using two-dimensional Gaussian surfaces.

The method for achieving polarisation in this model is quite different to that of Model A. Here, polarisation is

due to the reduced flux coming from the continuum so that, unlike Model A, a linear increase in absorption will not create a linear increase in polarisation. For this reason, absorption values of 77%, 91% and 97% were chosen so as to represent the same mean polarisation values used in Model A. To generate this source, the continuum region flux is diminished in accordance with the absorption value and then split between two images. The scattering region is then added to each image so that they satisfy Equation 6 for a constant polarisation of 20%. In addition, the relative flux of the two sources can then be set by the requirement that the polarisation at 0% absorption is 2% (this then increases non-linearly to 20% polarisation at 100% absorption).

### 3.3 Convolution

In order to determine the magnification distributions of the various source images, these images need to be convolved with the magnification maps. In doing this it was important to ensure that the physical scale corresponding to the pixel length of both source and magnification map was identical. For Model A this was determined by the design of the source, requiring a magnification map of  $2.136 \times 2.136ER$  ( $1024 \times 1024$  pixels). As this region is reasonably small it was important to recognise that a number of magnification maps would need to be used to obtain data (see Section 3.1). Neglecting this could reveal incorrect trends in any correlation data (in particular it would reduce the range of magnifications significantly). For this study, two maps of varying mean magnification were used to ensure that possible trends at both large and small magnification would not be overlooked (e.g. a trend at low magnification might be overlooked if dealing with a magnification map excessively covered with intense caustic structures); this is discussed further in Section 4.1. Note that this problem does not exist for Model B because the map is large enough that, on the whole, it is reasonably homogeneous and so has a mean that approaches the theoretical expectation value. As mentioned previously, the process for Model B was the reverse of that for Model A, whereby the largest magnification map of  $100 \times 100ER$  was created in order for the source to then integrate with it.

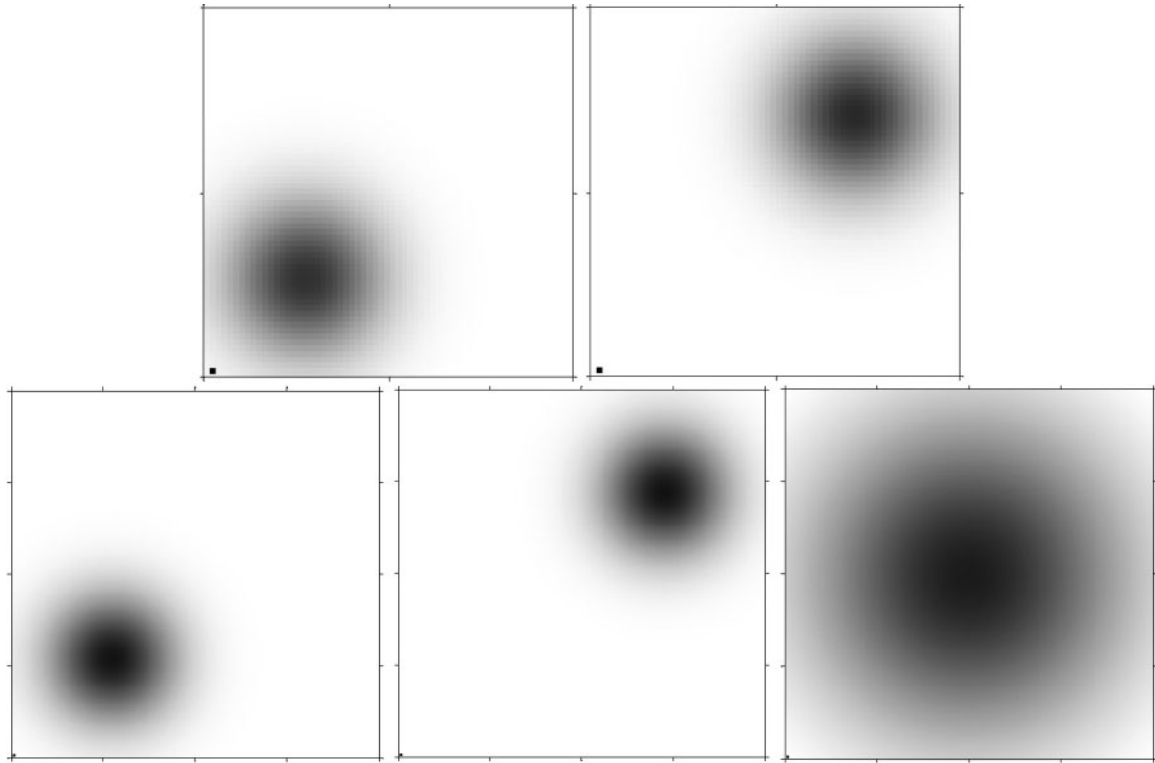


**Figure 5** This shows the five different sources considered as part of Model B at high absorption percentages (so that the continuum does not drown out the scattering region in the images). Scattering region radii are  $3.00 \times 10^{16}$  cm with separation distances of  $6.03 \times 10^{16}$  (top left) and  $1.66 \times 10^{17}$  cm (top right),  $7.70 \times 10^{16}$  cm with separation distances of  $2.00 \times 10^{17}$  cm (bottom left) and  $5.39 \times 10^{17}$  cm (bottom middle), and  $2.00 \times 10^{17}$  cm with a separation distance of  $3.70 \times 10^{17}$  cm (bottom right). Images in the top row have side length  $1.71 \times 10^{17}$  cm whereas images in the bottom row have side length  $5.34 \times 10^{17}$  cm. Note the continuum in the bottom-left corners.

In order to determine the polarisation following convolution (using the two polarised images formed for Model A or B) Equation 6 was used. These values could then be compared directly with the magnification values obtained from convolving the magnification map with an unabsorbed, unpolarised version of the corresponding source (these values were divided by the mean flux of the original source in order to obtain the correct magnification values). Correlation maps could then be obtained. Finally, note that for this paper all convolutions were computed without any zero-padded edges, so that areas contaminated by the overlaps were neglected.

#### 4 Results

Before looking at any correlation data it is insightful to look at the light curves to see just how the mean magnification and polarisation vary, as shown in Figures 6 and 7. These light curves are generated by taking a slice through the convolved data, representing what an observer would see as caustics pass over the source.

The time scales shown in these figures have been calculated using Equation 7, where the scale size of the source is  $f_{15} \times 10^{15}$  cm,  $z_1$  is the redshift of the lensing galaxy ( $z \sim 1.55$ ), and  $300v_{300}$  km  $s^{-1}$  is the velocity of the microlensing stars across the line of sight (Lewis & Belle 1998).

$$\tau \approx \frac{f_{15}}{1+z_1} \frac{D_1}{D_s} \frac{1}{v_{300}} \text{year} \quad (7)$$

However, it is worth noting that the uncertainty in the redshift of the lensing galaxy results in an uncertainty on the Einstein radius in the source plane and hence the physical size of the inferred absorption and scattering regions. In considering potential lens redshifts between  $z=1$  and  $z=2$  (assuming the cosmology from Section 3.1) it can be shown that the size of the Einstein radius varies roughly linearly between +30% and -30% of the value at  $z \sim 1.55$ . In other words the time scales shown in Figures 6 and 7 would vary by these same percentages.

These results hint at some interesting correlations between magnification and polarisation. In Model A, the polarisation fluctuations tend to occur at caustic crossings and the polarisation seems to oscillate about a mean value. In Model B it is seen that decreases in polarisation tend to occur at higher magnification and without any significant oscillation. This can be seen in the top image of Figure 7, whereby the polarisation during each microlensing event decreases significantly rather than oscillating about any particular value. With regard to possible observational testing this last point is of crucial significance because it indicates that as few as one major microlensing event may be used to differentiate between the two models. It is also worth noting that the same number of microlensing magnification events can be statistically expected for both models within a 20-year period, with this being related to the time taken for caustic structures

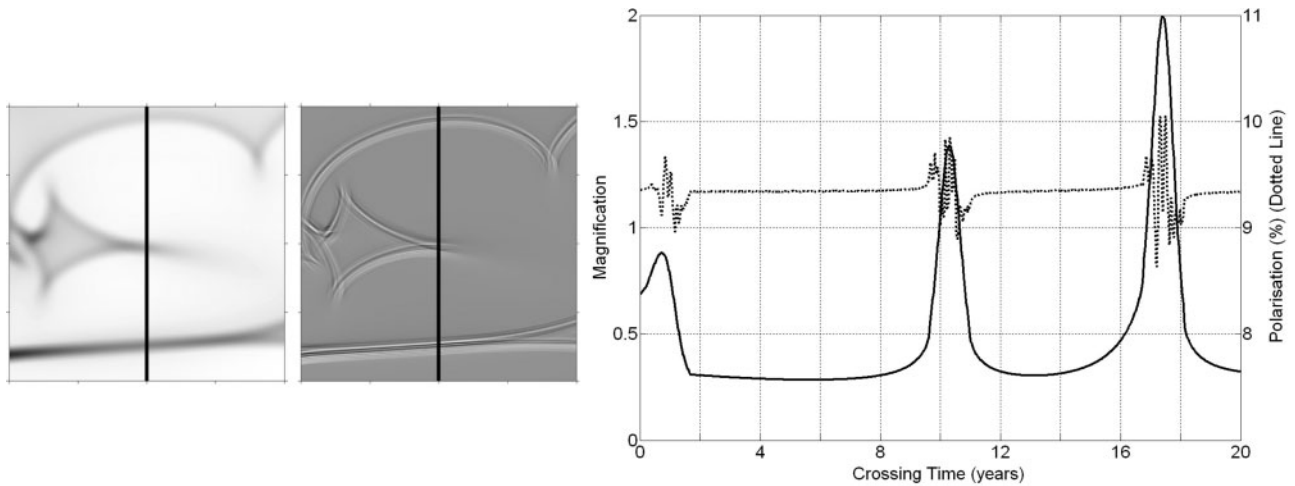


**Figure 6** Model A. Left: Convolution of unabsorbed source with  $2.136 \times 2.136ER$  magnification map ( $\sigma = \gamma = 0.4$ ). Middle: Resultant polarisation after application of Equation 6 to two convolutions of the polarised source (absorption = 50%, width = 50%). Both have side length  $5.47 \times 10^{16}$  cm. Right: Light curves for magnification and polarisation, as indicated by line from top to bottom in previous images.

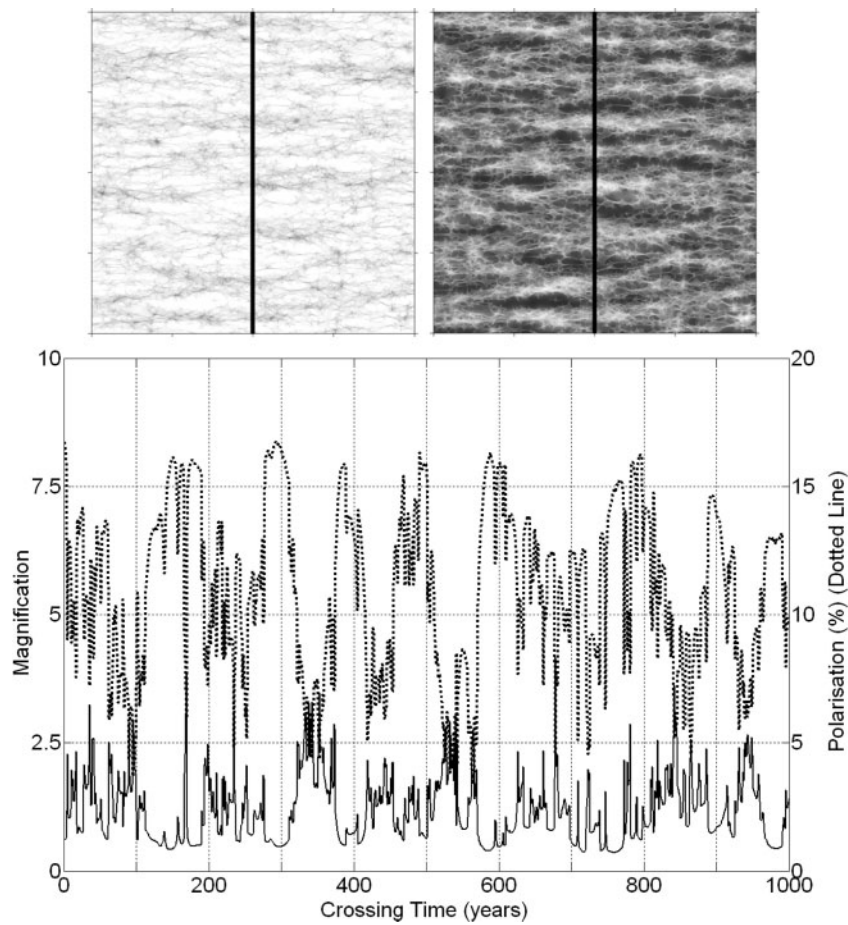


**Figure 7** Model B. Top Left: Convolution of unabsorbed source with  $100 \times 100ER$  magnification map (scattering region radius =  $3 \times 10^{16}$  cm, separation distance =  $1.66 \times 10^{17}$  cm and  $\sigma = \gamma = 0.4$ ). Top Middle: Resultant polarisation after application of Equation 6 to two convolutions of the polarised source (absorption = 91%). Both have side length  $2.56 \times 10^{18}$  cm. Top Right: Zoomed in view of bottom plot, corresponding to first 100 years. Bottom: Light curves for magnification and polarisation, as indicated by line from top to bottom in top left and top middle images. Note that the axes are slightly different to those in Figure 6.

to sweep the continuum source. As we will show in the next section, these trends are confirmed in an analysis of the correlations between magnification and polarisation for a large sample of microlensing scenarios.

#### 4.1 Trends in Model A

The correlations between polarisation and magnification for the scenarios described in Section 3.2.2 are shown in Figure 8 each panel presents a grey scale map of relative probability, with the continuum magnification on the  $x$ -axis and the degree of polarisation on the  $y$ -axis. Hence this shows trends between any fluctuations in the two. Before discussing the trends seen it should be noted that the apparent decrease in mean polarisation with increased absorption width (in this model) is in fact an artifact of the computational model. This artifact does not influence the overall trends obtained.

Firstly, it is apparent that the choice of matter distribution parameters for the lensing galaxy (i.e.  $\sigma$  and  $\gamma$ ) do not significantly affect the trends seen in these probability distributions (especially with the knowledge that any real data would be both incomplete and have error associated with it — only the most general of trends would be noticeable). The same can be generally said for the choice of cloud size, although it can be seen that the range of polarisations observed at any particular value of magnification decreases with decreasing cloud size. It is also worth noting that the choice of mean absorption does not induce any trends into the data apart from an obvious increase in mean polarisation, indicating that possible spectropolarimetric monitoring would not reveal different trends at different wavelengths within the CIV trough (recall Equation 4). In addition, by using two sets of data for each correlation map (corresponding to a small and large mean for the magnification map used, see Section 3.3), as seen more noticeably for the cases where  $n = 1$  and  $\omega = 50\%$ , it can be seen that the overall trends developed do not alter with lower or higher magnification.

All of the scenarios tested seem to support the general trend that an increase in magnification of the continuum flux (i.e. the unabsorbed continuum) will not indicate an increase or decrease in mean polarisation, but rather that the polarisation will remain reasonably constant throughout any microlensing activity. For all cases it is clear that increasing the width of absorption will increase the range of polarisations found at any particular magnification (the largest ranges are found around a magnification of 1, which of course is the approximate mean value of the magnification map). This then implies that if the source was observed over several months, the largest range of polarisations measured would have been occurring when the mean magnification of the continuum flux was around the theoretical mean. In other words, provided this model represents the view of the quasar, then the largest fluctuations in polarisation would occur when the continuum flux was at its time-averaged mean.

#### 4.2 Trends in Model B

The correlations between polarisation and magnification for the scenarios described in Section 3.2.3 are shown in Figure 9. It is immediately apparent that the trends seen in this model are very different from those seen in Model A, and at low magnification (for all scenarios tested), the polarisation values are much greater than at higher magnifications. Not surprisingly this is because of the geometry of the source as only the continuum source is strongly magnified, whereas the scattering region is effectively immune to the influence of the microlenses.

As with Model A, differences between mass distribution parameters for the lensing galaxy do not significantly affect the overall trends seen in the data. However, unlike Model A it can be seen that the choice of mean absorption does introduce a specific trend (other than simply increasing the mean polarisation); namely that at low absorption the mean polarisation drops with increasing magnification while at higher absorption the mean polarisation tends not to drop as much. In fact, at very high absorption this correlation begins to look like a horizontal line. This is illustrated further in Figure 10 (as per a row of Figure 9) for  $\sigma = \gamma = 0.4$  (this trend is the same for the other mass distributions), where absorption is now 99.7% (corresponding to a wavelength of  $\sim 1530 \text{ \AA}$ ). This result is important because it indicates that spectropolarimetric monitoring *would* reveal different trends at different wavelengths within the CIV trough.

Finally, it can be seen that by increasing the size of the scattering region the relationship between magnification and polarisation becomes more one-to-one (less broad). This occurs because, as the ratio between continuum and scattering region scale sizes decreases, the unpolarised continuum is allowed to be magnified in a more dominant manner thus reducing the overall polarisation. It can also be seen that variation in the separation distance between continuum and scattering region centre does not introduce any significant trends into the data. This makes sense, because as soon as these two regions are asymmetrically separated by at least the width of a caustic then the manner in which they are magnified becomes independent, yielding the similar results seen here.

## 5 Conclusions

This study has investigated the role that microlensing can play in differentiating between two popular models of how quasar BAL troughs are polarised. Using the macrolensed and microlensed quasar H1413+1143 as a case study, two computational models of polarisation were developed in order to investigate how magnification and polarisation variation detected by an observer could be used to differentiate between them. The results showed that the correlations between these two observables would be easily discernible between models. Two main differences were identified; for Model A, during a single microlensing magnification event, the polarisation at any wavelength within the CIV trough was seen

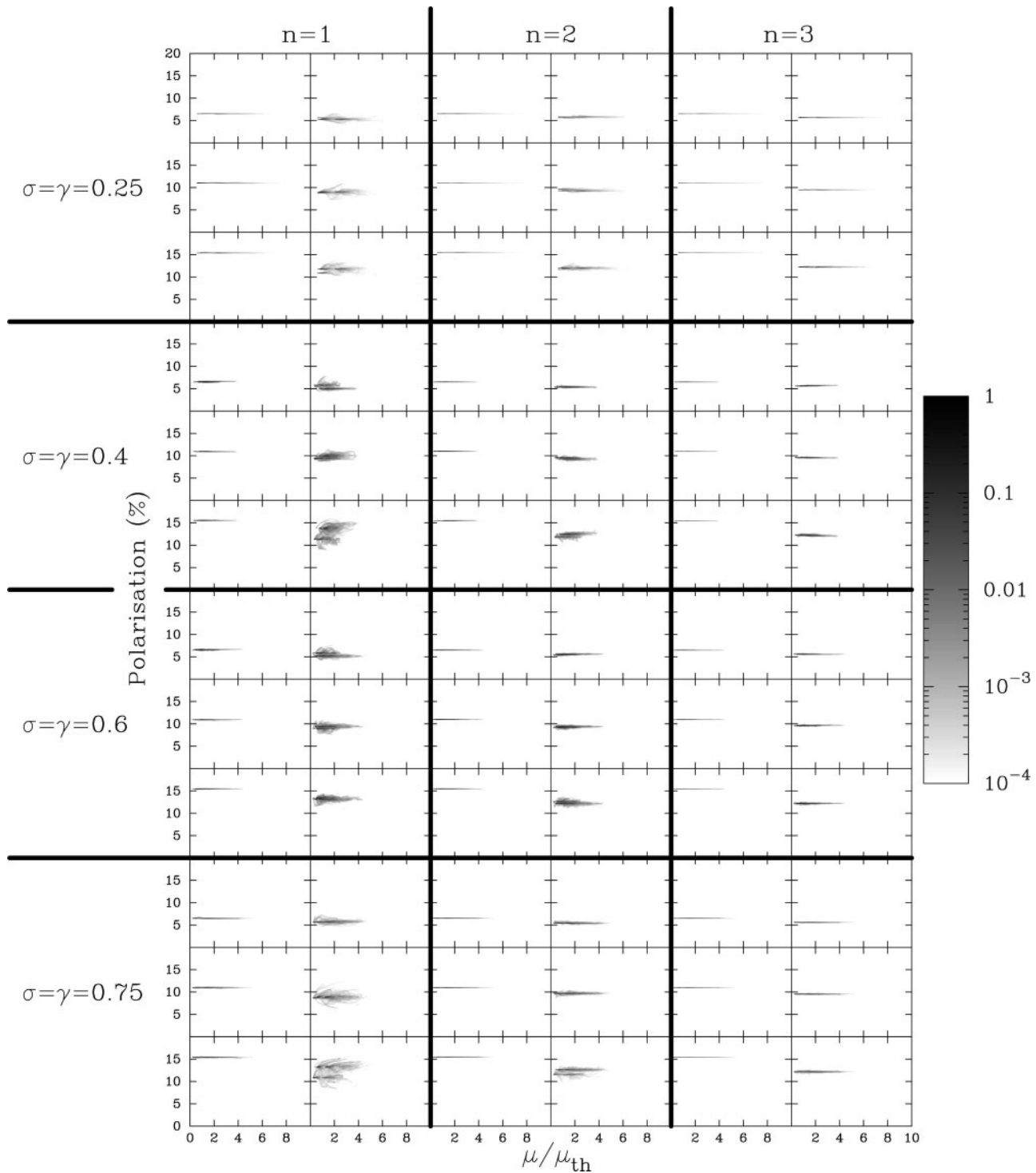


**Figure 8** Correlations for Model A. Note that the scale reflects relative probability as denoted by the grey-scale on the right of the figure. Each group of 6 maps represent mean absorption at 25% (top two), 50% (middle two) and 75% (bottom two), with an absorption width of 5% (left three) and 50% (right three). For each image the vertical axis shows polarisation while the horizontal axis shows magnification (this has been normalised with respect to the theoretical mean magnification  $\mu_{th}$  (see Equation 3)).

to oscillate about a mean value, while away from high magnification events the polarisation was found to be relatively constant. This was found to be in stark contrast with Model B, whereby the mean polarisation at any particular wavelength within the trough was found to rise and fall in anti-correlated fashion with magnification. The second main difference was that if polarisation and magnification

variation were monitored at various wavelengths within the CIV trough, then significantly different trends would be seen in this data between wavelengths for Model B but not Model A. Hence spectropolarimetric monitoring through even a single high magnification event would provide constraints on the underlying scattering geometry. Given that caustic crossing times for H1413+1143 would be of

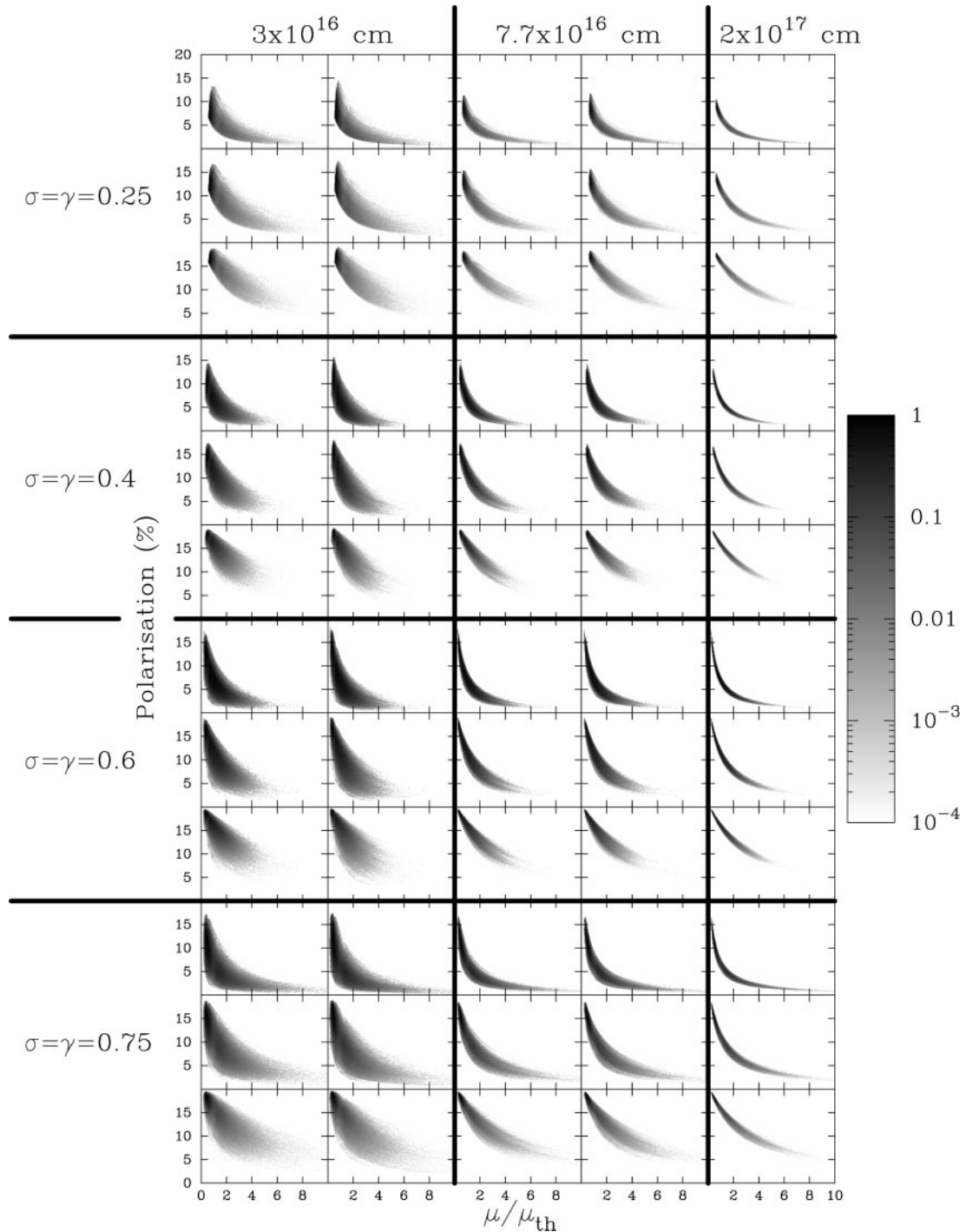


**Figure 9** Correlations for Model B. The images along each row represent the 5 scenarios presented in Figure 5, namely a scattering region radius of  $3 \times 10^{16}$  cm with a separation distance of  $6.03 \times 10^{16}$  and  $1.66 \times 10^{17}$  cm,  $7.7 \times 10^{16}$  cm with a separation distance of  $2.00 \times 10^{17}$  and  $5.39 \times 10^{17}$  cm, and  $2 \times 10^{17}$  cm with a separation distance of  $3.70 \times 10^{17}$  cm. Rows are then arranged in threes, representing absorption at 77% (top), 91% (middle) and 97% (bottom). For each image the vertical axis shows polarisation while the horizontal axis shows magnification.

order months to years, an observational campaign monitoring this system on a weekly to monthly basis would be required to differentiate between the two models. Note however that spectropolarimetric monitoring is required for high magnification events and an observational program to obtain high temporal sampling could be triggered based on simple photometric monitoring of the images.

In addition, through the larger variations in polarisation seen for all modelled scenarios of Model B, this study supports recent data for H1413+1143 (Chae et al. 2001; Chartas et al. 2004) which also suggests that a scattering region is most likely responsible for the increased polarisation found in BAL troughs. Such increased variation comes about in this model because the continuum region

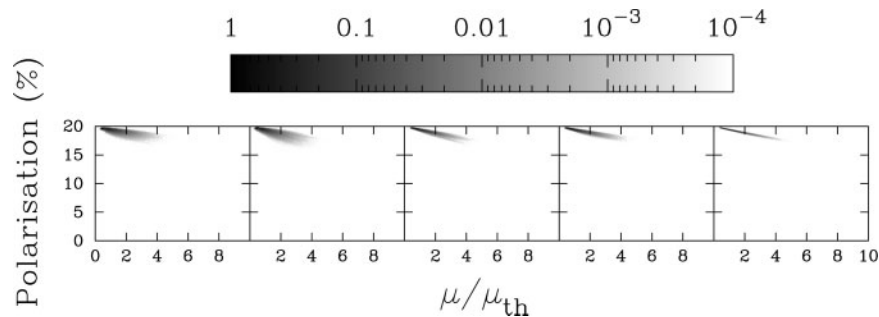


**Figure 10** Correlations for Model B. Same as the  $\sigma = \gamma = 0.4$  rows of Figure 9, but with each image at 99.7% absorption.

would be much more susceptible to microlensing than the larger scattering region. If this scenario is correct, then this hints that such a scattering region is also operating in other such quasars. For further work, the detailed temporal properties of the expected polarisation fluctuations need to be determined with the goal of developing the most efficient observational strategy to observe microlensed BAL quasars.

### Acknowledgements

The anonymous referee is thanked for comments that improved the clarity of this paper. This research was undertaken as a third year special project at the University of Sydney.

### References

- Abajas, C., Mediavilla, E., Muñoz, J. A., Popović, L. Č. & Oscoz, A., 2002, *ApJ*, 576, 640
- Angonin, M.-C., Vanderriest, C., Remy, M. & Surdej, J., 1990, *A&A*, 233, L5
- Antonucci, R., 1993, *ARA&A*, 31, 473
- Antonucci, R. R. J. & Miller, J. S., 1985, *ApJ*, 297, 621
- Becker, R. H., Gregg, M. D., Hook, I. M., McMahon, R. G., White, R. L. & Helfand, D. J., 1997, *ApJ*, 479, L93
- Belle, K. E. & Lewis, G. F., 2000, *PASP*, 112, 320
- Blandford, R. D., Netzer, H. & Woltjer, L., 1990, *Active Galactic Nuclei* (New York: Springer-Verlag)
- Brandt, W. N., Comastri, A., Gallagher, S. C., Sambruna, R. M., Boller, T. & Laor, A., 1999, *ApJ*, 525, L69
- Cattaneo, A., 2002, *MNRAS*, 333, 353
- Chae, K.-H., Turnshek, D. A., Schulte-Ladbeck, R. E., Rao, S. M. & Lupie, O. L., 2001, *ApJ*, 561, 653
- Chang, K. & Refsdal, S., 1979, *Natur*, 282, 561
- Chantry, V. & Magain, P., 2007, preprint (astro-ph/0612094)
- Chartas, G., Eracleous, M., Agol, E. & Gallagher, S. C., 2004, *ApJ*, 606, 78
- Chwolson, O., 1924, *AN*, 221, 329
- Cohen, M. H., Ogle, P. M., Tran, H. D., Vermeulen, R. C., Miller, J. S., Goodrich, R. W. & Martel, A. R., 1995, *ApJ*, 448, L77
- Fender, R., Wu, K., Johnston, H., Tzioumis, T., Jonker, P., Spencer, R. & van der Klis, M., 2004, *Natur*, 427, 222
- Gallagher, S. C., Brandt, W. N., Sambruna, R. M., Mathur, S. & Yamasaki, N., 1999, *ApJ*, 519, 549
- Goodrich, R. W. & Miller, J. S., 1995, *ApJ*, 448, L73
- Gould, A. & Miralda-Escudé, J., 1997, *ApJ*, 483, L13
- Hawkins, M. R. S. & Taylor, A. N., 1997, *ApJ*, 482, L5
- Hewett, P. C. & Foltz, C. B., 2003, *AJ*, 125, 1784
- Hutsemékers, D., 1993, *A&A*, 280, 435
- Kaspi, S., Smith, P. S., Netzer, H., Maoz, D., Jannuzi, B. T. & Giveon, U., 2000, *ApJ*, 533, 631
- Kayser, R., Surdej, J., Condon, J. J., Kellermann, K. I., Magain, P., Remy, M. & Smette, A. 1990, *ApJ*, 364, 15
- Kneib, J.-P., Alloin, D. & Pello, R., 1998, *A&A*, 339, L65
- Kuncic, Z., 1999, *PASP*, 111, 954
- Lamy, H. & Hutsemékers, D., 2004, *A&A*, 427, 107
- Lewis, G. F. & Belle, K. E., 1998, *MNRAS*, 297, 69
- Lewis, G. F. & Ibata, R. A., 2004, *MNRAS*, 348, 24
- Magain, P., Surdej, J., Swings, J.-P., Borgeest, U. & Kayser, R., 1988, *Natur*, 334, 325
- Murray, N. & Chiang, J., 1998, *ApJ*, 494, 125
- Murray, N., Chiang, J., Grossman, S. A. & Voit, G. M., 1995, *ApJ*, 451, 498
- Ogle, P. M., 1997, *ASPC* 128, *Mass Ejection from Active Galactic Nuclei*, Eds. Aravn, N., Shlosman, I. & Weymann, R. J. (San Francisco: Astronomical Society of the Pacific), 78
- Østensen, R., et al., 1997, *A&AS*, 126, 393
- Rees, M. J., 1984, *ARA&A*, 22, 471
- Reichard, T. A., et al., 2003, *AJ*, 126, 2594
- Schmidt, G. D. & Hines, D. C., 1999, *ApJ*, 512, 125
- Schneider, P., Ehlers, J. & Falco, E. E., 1999, *Gravitational Lenses* (New York: Springer-Verlag)
- Spergel, D. N., et al., 2007, *ApJ*, in press (astro-ph/0603449)
- Turnshek, D. A., 1984, *ApJ*, 280, 51
- Turnshek, D. A., 1995, *ESO Workshop, QSO Absorption Lines*, Ed. Meylan, G. (Berlin: Springer), 223
- Turnshek, D. A., Lupie, O. L., Rao, S. M., Espy, B. R. & Sirola, C. J., 1997, *ApJ*, 485, 100
- Wambsganss, J., 1990, Ph.D. Thesis (Garching: Max Planck Institut)
- Wambsganss, J., 1992, *ApJ*, 392, 424
- Wambsganss, J., 1998, *LRR*, 1, 12
- Wambsganss, J. & Paczynski, B., 1991, *AJ*, 102, 864
- Wambsganss, J., Schneider, P. & Paczynski, B., 1990, *ApJ*, 358, L33
- Wang, H.-Y., Wang, T.-G. & Wang, J.-X., 2005, *ApJ*, 634, 149
- Weymann, R., 1995, *ESO Workshop, QSO Absorption Lines*, Ed. Meylan, G. (Berlin: Springer), 213
- Witt, H. J. & Mao, S., 1994, *ApJ*, 429, 66
- Wyithe, J. S. B. & Loeb, A., 2002, *ApJ*, 577, 615